

Atomic Insights into the Enhanced Surface Stability in High Voltage Cathode Materials by Ultrathin Coating

Xin Fang, Feng Lin, Dennis Nordlund, Matthew Mecklenburg, Mingyuan Ge, Jiepeng Rong, Anyi Zhang, Chenfei Shen, Yihang Liu, Yu Cao, Marca M. Doeff, and Chongwu Zhou*

Surface properties of electrode materials play a critical role in the function of batteries. Therefore, surface modifications, such as coatings, have been widely used to improve battery performance. Understanding how these coatings function to improve battery performance is crucial for both scientific research and applications. In this study the electrochemical performance of coated and uncoated $\text{LiNi}_{0.5}\text{Mn}_{1.5}\text{O}_4$ (LNMO) electrodes is correlated with ensemble-averaged soft X-ray absorption spectroscopy (XAS) and spatially resolved scanning transmission electron microscopy-electron energy loss spectroscopy (STEM-EELS) to illustrate the mechanism of how ultrathin layer Al_2O_3 coatings improve the cycle life of $\text{LiNi}_{0.5}\text{Mn}_{1.5}\text{O}_4$. Mn^{2+} evolution on the surface is clearly observed in the uncoated sample, which results from the reaction between the electrolytic solution and the surfaces of $\text{LiNi}_{0.5}\text{Mn}_{1.5}\text{O}_4$ particles, and also possibly atomic structure reconstructions and oxygen loss from the surface region in $\text{LiNi}_{0.5}\text{Mn}_{1.5}\text{O}_4$. The coating effectively suppresses Mn^{2+} evolution and improves the battery performance by decelerating the impedance buildup from the surface passivation. This study demonstrates the importance of combining ensemble-averaged techniques (e.g., XAS) with localized techniques (e.g., STEM-EELS), as the latter may yield unrepresentative information due to the limited number of studied particles, and sheds light on the design of future coating processes and materials.

stringent, especially in terms of energy density and cycle life. In this respect, further improvement and precise understanding of batteries are highly desired and urgently needed. Since the total energy of a battery is dependent both upon cell voltage and capacity, increasing the output voltage is an important method to enhance the energy of batteries.^[2] According to Goodenough,^[3] the spinel $\text{LiNi}_{0.5}\text{Mn}_{1.5}\text{O}_4$ is electroactive at the upper voltage limit of compatibility with organic carbonate electrolytic solutions. Since the potential profile is nearly flat in spite of the two-electron change in the Ni redox state, which is highly desirable for power management, $\text{LiNi}_{0.5}\text{Mn}_{1.5}\text{O}_4$ is considered one of the most promising high voltage cathode materials for lithium ion batteries.^[3,4]

Surface properties are critical to the functioning of battery materials in many aspects, as solid electrolyte interfaces and cathode electrolyte interfaces (CEI) influence cyclability and rate capability.^[5,6] Surface coatings have been recognized as an effective method to control and optimize the surface properties of both

cathode and anode materials in batteries and are widely utilized in both academic research and industry applications.^[7,8] However, the quality of surface coatings depends critically on the properties of the coating and active materials as well as the processes used. The effect of many types of surface coatings on $\text{LiNi}_{0.5}\text{Mn}_{1.5}\text{O}_4$, used to ameliorate the side reactions during the high voltage operation, including materials such

1. Introduction

Lithium ion batteries have been widely recognized as the most important energy storage devices and power sources for portable electronics.^[1] Nowadays, with the development of new-generation electronic devices and more importantly, electric vehicles, performance requirements have become more

Dr. X. Fang, Dr. M. Ge, Dr. J. Rong, A. Zhang, C. Shen, Prof. C. Zhou
Mork Family Department of Chemical Engineering and Materials Science
Los Angeles, CA 90089, USA
E-mail: chongwuz@usc.edu

Prof. F. Lin, Dr. M. M. Doeff
Energy Storage and Distributed Resources Division
Lawrence Berkeley National Laboratory
Berkeley, CA 94720, USA

Prof. F. Lin
Department of Chemistry
Virginia Tech
Blacksburg, VA 24061, USA

Dr. D. Nordlund
Stanford Synchrotron Radiation Lightsource
SLAC National Accelerator Laboratory
Menlo Park, CA 94025, USA

Dr. M. Mecklenburg
Center for Electron Microscopy and Microanalysis
University of Southern California
Los Angeles, CA 90089, USA

Y. Liu, Y. Cao, Prof. C. Zhou
Ming Hsieh Department of Electrical Engineering
University of Southern California
Los Angeles, CA 90089, USA



DOI: 10.1002/adfm.201602873

as Au,^[9] Ag,^[10] Bi₂O₃,^[6] BiOF,^[11] ZnO,^[12,13] ZrO₂,^[14] ZrP₂O₇,^[14] AlF₃,^[15] conductive carbon,^[16] polyimide,^[17] graphene oxide,^[18] and coating processes such as wet chemistry,^[6,17] sputtering,^[10] evaporation,^[9] and atomic layer deposition (ALD),^[19,20] have led to varying results. In addition, much of the previous work only demonstrated improved cycling and/or rate performance with limited in-depth exploration of the mechanism of the improvement; thus the knowledge to guide future work is unclear. The few existing mechanistic studies mainly focused on one charge–discharge cycle whereas the cumulative effect during long-term cycling has rarely been considered. It is important to investigate the function of coating materials and coating processes in order to better understand the mechanism of improved battery performance by surface modification and provide insights for the further advancement of high performance batteries.

Here, we report our investigations on the surface properties of LiNi_{0.5}Mn_{1.5}O₄ and reveal how ultrathin layers of Al₂O₃ coated by ALD improved the cycling stability. We have correlated the battery performance shown in the electrochemical measurements with results from ensemble-averaged X-ray absorption spectroscopy (XAS) and spatially resolved STEM-EELS. The analysis provides insights into the evolution of Mn²⁺ on the surface of LiNi_{0.5}Mn_{1.5}O₄ and the function of the metal oxide coating in suppressing this undesired surface reaction, which leads to impedance buildup. The discovery in our work provides guidelines for prospective studies on the possibility of improving battery performance through surface property tuning and ultrathin coatings down to the atomic scale. More importantly, since many materials have similar surface phenomena such as chemical evolution and surface reconstruction, the research methodology and mechanism illustrated in this

work provides insightful information that can be beneficial to studies on other electrode materials.

2. Results and Discussion

2.1. Precycling Characterization

LiNi_{0.5}Mn_{1.5}O₄ particles can be synthesized via various methods, with coprecipitation and solid-state reactions the most relevant choices for industrial applications. Here we synthesized LiNi_{0.5}Mn_{1.5}O₄ particles using a solid-state reaction as reported in our previous work.^[19,21] **Figure 1a** shows the scanning electron microscope image of the as-synthesized LiNi_{0.5}Mn_{1.5}O₄ particles. The particles had polyhedral shapes with sizes ranging from around 1 to 2 μm. The X-ray diffraction (XRD) pattern of the as-synthesized LiNi_{0.5}Mn_{1.5}O₄ particles is presented in the inset of **Figure 1a**. All the peaks can be indexed according to the reported pattern for cubic structured spinel LiNi_{0.5}Mn_{1.5}O₄.^[22]

As illustrated in the schematic diagram **Scheme 1**, Al₂O₃ was coated on prefabricated electrodes through ten cycles of ALD using the same process as reported in our previous work,^[19] with a growth rate of about 0.12 nm per cycle. ALD is known as the most favorable thin film technology for continuous and pin-hole free thin film deposition with precise thickness control. The self-limiting surface reaction leads to conformal coverage even on high aspect ratio structures.^[23] The particles here reflect the particles in the LiNi_{0.5}Mn_{1.5}O₄ electrode. **Scheme 1** shows that all the surface area that would be exposed to the electrolyte is covered by an Al₂O₃ film, while the conductive pathway inside the electrode is not blocked by the Al₂O₃

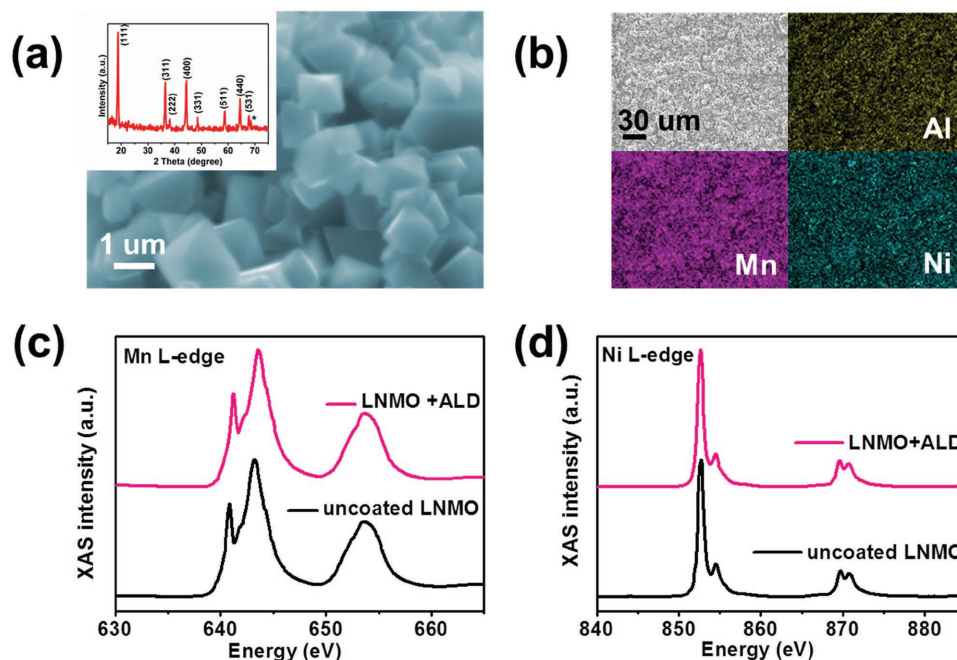
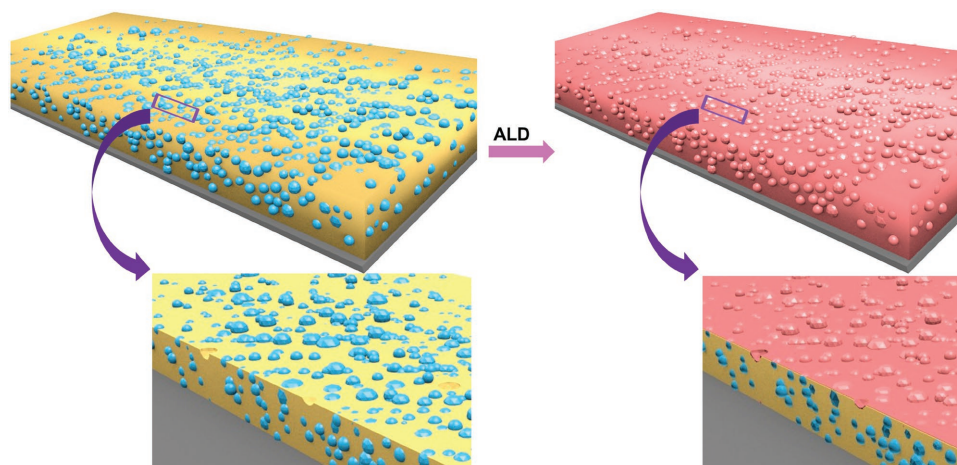


Figure 1. a) Scanning electron microscope image and (inset) XRD pattern of the as-synthesized LiNi_{0.5}Mn_{1.5}O₄ particles before ALD coating. b) EDX mapping of Al, Ni, and Mn on the surface of the electrode after ALD coating. The mapping area is shown in the upper left. XAS results of c) Mn and d) Ni of both coated and uncoated electrodes before cycling.



Scheme 1. Schematic diagram showing ALD on prefabricated electrodes.

film. Figure 1b shows the energy dispersive X-ray (EDX) mapping of the electrode surface where the evidence for the existence of Al is obviously seen, demonstrating successful coating of the samples. To confirm that the ALD process does not alter the oxidation states of transition metals on the surface, Mn and Ni oxidation states were probed by soft XAS for both coated and uncoated samples before cycling (Figure 1c,d). The total electron yield (TEY) mode, which has a depth sensitivity of 5–10 nm in this configuration, was used to obtain the data. The spectra are essentially identical, indicating no change to the Ni and Mn oxidation states after coating. The data are consistent with oxidation states of Mn and Ni that are primarily +4 and +2, respectively, as expected.^[24]

2.2. Electrochemical Characterization of Coated and Uncoated $\text{LiNi}_{0.5}\text{Mn}_{1.5}\text{O}_4$ Electrodes

To explore the mechanism of the enhanced cycling stability of $\text{LiNi}_{0.5}\text{Mn}_{1.5}\text{O}_4$, we looked into the changes of transition metal oxidation states after cycling, since the oxidation and reduction of transition metals are fundamental processes during cell operation. Before taking the XAS measurements, both the coated and uncoated electrodes were cycled at C/5 between 3.5 and 5.0 V for 35 cycles in CR2032 size coin cells with lithium metal as the counter electrodes. Representative charge–discharge curves are plotted in Figure 2a,c. The coated and uncoated electrodes were prepared from the same batch of material and underwent the same charging profile, so the difference in cycling stability can be attributed to the coating process. In both cases, a small amount of capacity near 4 V suggests that some Mn^{3+} was present in the as-made material, although most of the redox activity took place at about 4.7 V, as is typical for $\text{LiNi}_{0.5}\text{Mn}_{1.5}\text{O}_4$.^[24,25] Here it is clearly seen that after only 35 cycles at C/5, the uncoated samples show a capacity loss while the coated ones showed much better capacity retention and coulombic efficiency after the first cycle (≈ 98.8 vs 98.2%, Figure S1, Supporting Information). The difference is more obvious when the cells are cycled at C/2; see the representative profiles in Figure 2b,d. With the increased rate (C/2 compared

with C/5), the differences in polarization for both charge and discharge processes between the two types of electrodes are clearly observed. Moreover, the increase in overpotential became more evident for the uncoated electrode as the cycling progressed, compared to the coated electrode. Further evidence for this is the voltage gap between the charge and discharge profiles at 60 mAh g^{-1} in Figure 2b,d. These are plotted in Figure 2e. It is clear that there is a much larger gap for the cells containing the uncoated samples compared to those with the coated ones and that the polarization rises more rapidly with cycle number. The rise in overpotential caused an apparent capacity decay when the cell was cycled, due to the limited voltage window, and suggests that there was a rise in impedance.^[26] To verify this, electrochemical impedance spectra (EIS) were measured before cycling (shown in Figure S2, Supporting Information) and after set numbers of cycles at C/5 at 4.7 V for cells in the charged state; see Figure 2f. The plots in the figure correspond to 1st cycle, 10th cycle, 25th cycle, and 35th cycle, respectively. An increase in charge transfer resistance during cycling can be clearly seen but the increase in uncoated sample is obviously larger than the coated one. Compared to the data for the cell with the coated sample, the larger semicircle radius seen in the high frequency part of the Nyquist plot of the cell with the uncoated sample suggests that there is higher charge transfer resistance for the latter.^[12,27] The results here are also consistent with our previous EIS study on the cells cycled at C/2.^[19] The charge transfer resistance is related to surface properties of the electrodes and an increase is associated with deterioration of battery performance. The impedance and overpotential data demonstrate that an ultrathin surface modification with Al_2O_3 can effectively suppress the increase in impedance of the batteries, and hence improve the battery performance. To obtain further insights related to the above phenomena, the surface properties of the electrodes were examined, as described below.

2.3. Postcycling Characterization

Because of the low penetration depth of soft X-rays, XAS can be an excellent tool for studying surface phenomena.^[28,29]

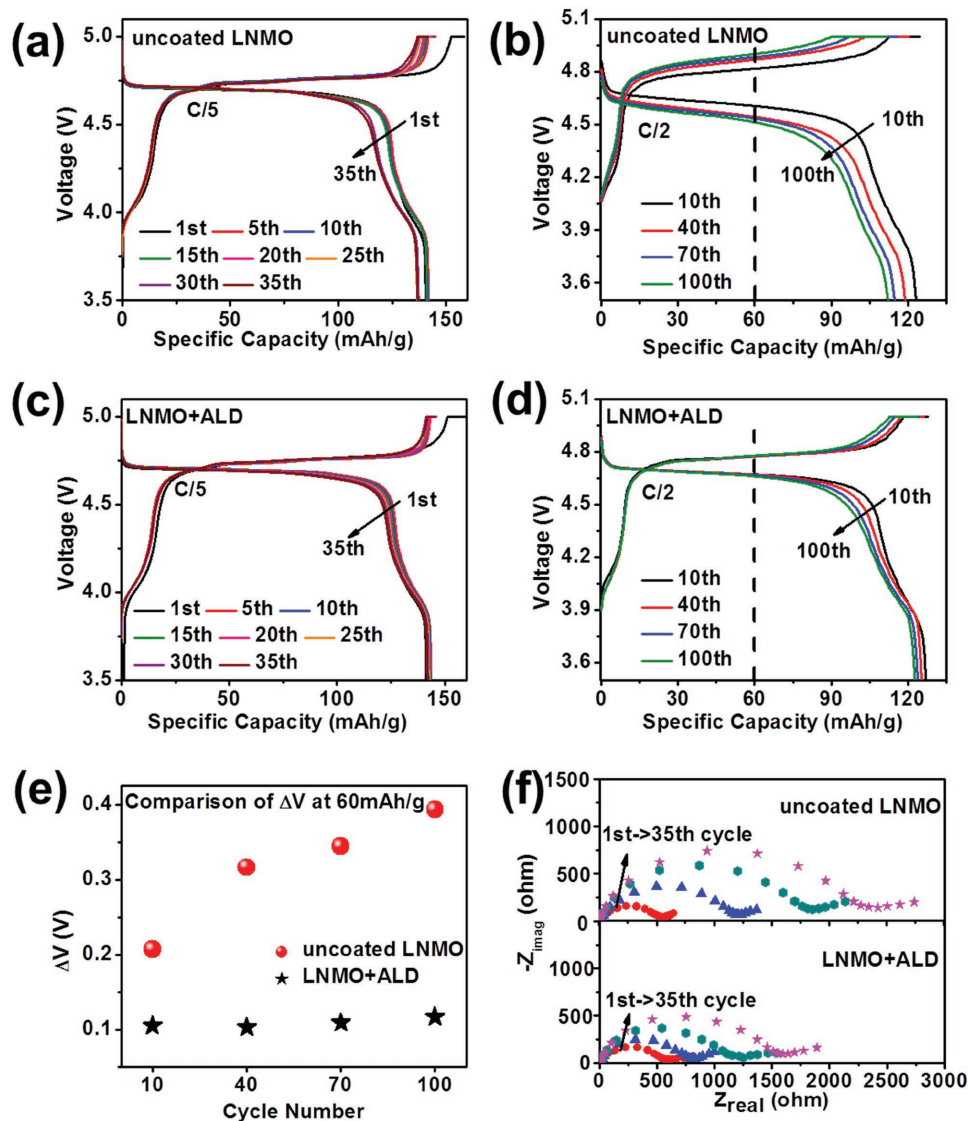


Figure 2. Representative charge–discharge curves of a,b) uncoated and c,d) coated $\text{LiNi}_{0.5}\text{Mn}_{1.5}\text{O}_4$ at C/5 and C/2 ($1\text{C} = 140\text{ mA g}^{-1}$). e) Comparison of voltage gap at 60 mAh g^{-1} of coated and uncoated electrodes at C/2. f) Comparison of Nyquist plots for cells containing coated and uncoated electrodes in the charged state from 1st cycle, 10th cycle, 25th cycle, and 35th cycle, respectively.

The transition metal L-edge XAS measures the electric dipole allowed electron transition from 2p to unfilled 3d orbitals. In this case, L-edge X-ray absorption spectra are ideal for studying the transition metal 3d states to examine their redox states. The L-edge spectra of Ni and Mn for both coated and uncoated samples after 35 cycles at C/5 are presented in Figure 3a,b. The spectra of the pristine samples are also provided for comparison.

From the Ni L-edge spectra in TEY mode, which probes about 5 nm deep from the surface, there is clear evidence for the oxidation of Ni from Ni^{2+} to Ni^{2+x} state after charging and reduction back to Ni^{2+} after discharging. The ratio of the intensities of the two peaks in the Ni L_3 region changed, with the higher frequency peak increasing upon oxidation and vice versa.^[30] This corresponds to the main reaction of $\text{LiNi}_{0.5}\text{Mn}_{1.5}\text{O}_4$, whose primary capacity comes from the $\text{Ni}^{2+}/\text{Ni}^{2+x}$ redox couple. The

results may be complicated by possible surface reactions of the nickel; in nickel-containing layered oxides, surface Ni is often found to be in a lower oxidation state than that in the bulk at the top of charge.^[30,31] A comparison of the Ni L_3 peak ratios in the spectra of the coated and uncoated $\text{LiNi}_{0.5}\text{Mn}_{1.5}\text{O}_4$ electrodes in the charged state shows a slightly higher Ni oxidation state in the former compared to the latter, judging from the peak at 854 eV (pointed out with arrows in Figure 3a). This suggests that the ALD coating provides some protection against the surface reconstruction phenomenon that leads to lower average oxidation states of transition metals on particle surfaces.

More interesting results are revealed in the spectra for the Mn L-edges. There is little difference between the coated and uncoated samples in the charged states. The spectra of the charged electrodes also look very similar to that of the electrodes in the pristine state, consistent with the fact that most of

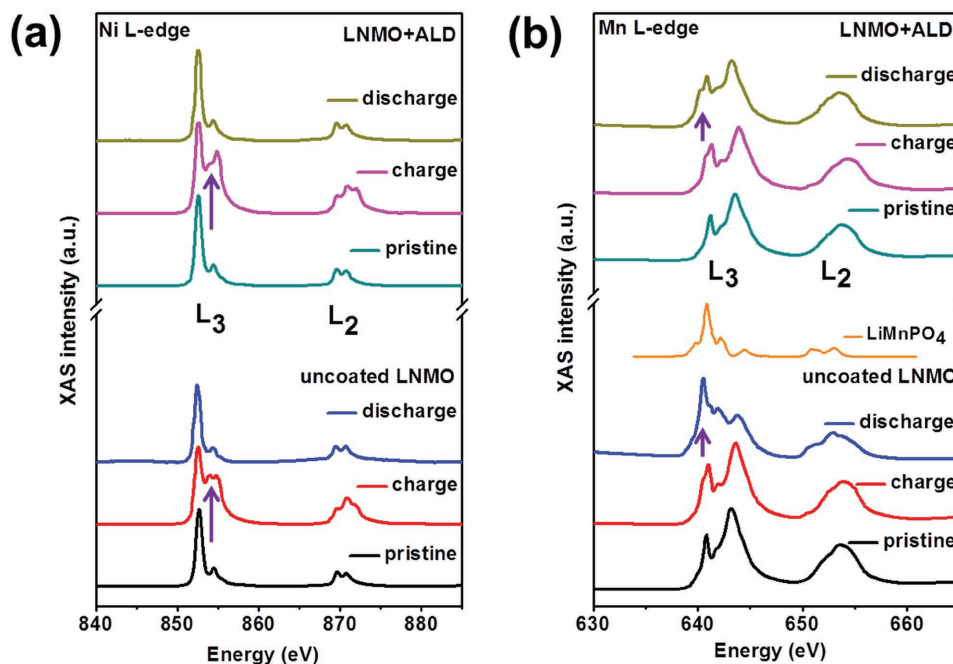


Figure 3. a) Ni L-edge XAS/TEY spectra for uncoated and coated electrodes. b) Mn L-edge XAS/TEY spectra for uncoated and coated electrodes. All spectra were collected from electrodes at the 35th cycle, in either the fully charged or fully discharged state, as noted in the figures. The electrodes in the charged state were taken out from batteries after the constant voltage charge step and the ones at discharged state were taken from batteries after constant current discharge to 3.5 V.

the Mn in $\text{LiNi}_{0.5}\text{Mn}_{1.5}\text{O}_4$ is not electroactive. However, the Mn L-edge spectra obtained on electrodes in the discharged state show distinct differences between the coated and uncoated samples, with far less Mn^{2+} appearing in the former, judging from the relative intensities at 640 eV (pointed out with arrows in Figure 3b). As a reference for Mn^{2+} octahedrally coordinated to oxygen, the Mn L-edge spectrum for LiMnPO_4 is also shown. The results indicate that Mn^{2+} is formed during the discharge process and is reoxidized during charge. With the ALD coating, the Mn^{2+} evolution is effectively suppressed. This is also consistent with the differences in coulombic efficiencies observed between the coated and uncoated samples, where the ALD coated samples showed slightly higher coulombic efficiency than the uncoated ones (≈ 98.8 vs $\approx 98.2\%$, Figure S1, Supporting Information).

In the literature, different $\text{LiNi}_{0.5}\text{Mn}_{1.5}\text{O}_4$ /electrolyte interface reactions have been reported by different groups with various measurements, including X-ray photoelectron spectroscopy (XPS), XAS, neutron reflectometry, optical fluorescence spectroscopy, and so on.^[32,33] Several Mn-related products were discovered and reported, such as MnF_2 , Mn^{2+} oxalates and carbonates, and $\text{Mn}^{2+/3+}$ complexes with β -diketonate ligands, although the exact reaction process is still unclear and under investigation.^[33,34] Qiao et al. have reported that Mn dissolution in $\text{LiNi}_{0.5}\text{Mn}_{1.5}\text{O}_4$ is correlated with electrolyte/electrode interactions rather than Mn^{3+} disproportionation.^[29] Jarry et al. also reported the formation of Mn containing species via reactions between the electrolyte and surfaces of $\text{LiNi}_{0.5}\text{Mn}_{1.5}\text{O}_4$ particles.^[33] The results here support the analysis that the main reason for the Mn^{2+} evolution is the reaction with electrolyte, rather than Mn^{3+} disproportionation, as the Mn^{3+} plateau did not

change much in the charge–discharge curves of the uncoated samples whereas the Mn^{2+} evolution is obvious. In the coated electrodes, all the surfaces exposed to electrolyte are covered with Al_2O_3 , since it is known that the ALD precursors can diffuse through the pores in the electrodes and conformally coat them.^[8] This inhibits direct contact between $\text{LiNi}_{0.5}\text{Mn}_{1.5}\text{O}_4$ and electrolyte suppressing the side reactions that form Mn^{2+} . As a result, the coated samples show much less Mn^{2+} evolution than the uncoated ones. In full cells with graphite anodes, Mn was found to deposit onto the anode causing deterioration of the performance, especially capacity decay and impedance buildup.^[33,35] Also, the Mn reduction and deposition on the anode leads to reduced coulomb efficiency. Thus, adding a conformal coating layer via ALD can be an effective strategy to enhance battery performance.

Besides Mn^{2+} formation and dissolution, it has also been reported that the transition metal ions in the surface region can migrate into the tetrahedral Li sites and empty octahedral sites upon cycling, resulting in the formation of Mn_3O_4 -like and rock-salt structures on the surface, accompanied by loss of surface oxygen.^[36] Mn^{2+} occupancy of the tetrahedral Li sites would lead to a Mn_3O_4 -like spinel structure in $\text{LiNi}_{0.5}\text{Mn}_{1.5}\text{O}_4$.^[37] The formation of the Mn_3O_4 -like and rock-salt structures on the surface is also related to the densification of the atomic structure and the buildup of charge transfer resistance.^[38,39]

As surface reconstruction is intrinsic to $\text{LiNi}_{0.5}\text{Mn}_{1.5}\text{O}_4$, as evidenced in literature,^[36,39] it will not be prevented by surface modifications such as coating, but surface modification can slow down the surface reconstruction. Since surface Mn_3O_4 is highly correlated to Mn^{2+} dissolution,^[40] we believe less Mn dissolution can induce less Mn migration in the lattice during

cycling, which can lead to a protection against the evolution of further structural transformation and buildup of resistance. Further in-depth study will be needed to gain advanced knowledge on this phenomenon and to guide future study surface modification strategies such as the fine tuning of coating thickness.

This also coincides with XPS and time-of-flight secondary ion mass spectrometry results in the recent literature showing that coatings can lead to thinner cathode-electrolyte interface layers.^[41] The obvious differences between the coated and uncoated electrodes seen in the XAS measurements implies that the increased impedance comes from surface reactions of the $\text{LiNi}_{0.5}\text{Mn}_{1.5}\text{O}_4$, and that the ultrathin layer of Al_2O_3 on electrode surfaces can effectively suppress this phenomenon to a large extent. We note here that there should be an optimized thickness of the coating layer especially when the coating material is an insulator such as Al_2O_3 . Thicker coatings might be more effective for surface modification but may also increase the electron transfer resistance and have a negative effect on the power performance of the batteries.^[19] The ability to exert good control over the thicknesses of the conformal coatings, even down to the atomic level, however, makes ALD an ideal process for fabricating protected electrodes.

XAS results are ensemble averaged and show signals from numerous particles in the electrodes. To obtain detailed information on individual particles, STEM imaging was performed. We investigated the surface Mn oxidation states of $\text{LiNi}_{0.5}\text{Mn}_{1.5}\text{O}_4$ particles in the discharged state after cycling,

using STEM-EELS. The EELS line scan profiles are shown in the STEM images for particles from both coated and uncoated samples in the right side of Figure 4a,b, with the first nine spectra from the very surface presented on the left side. The step sizes for the EELS scans are 1.5 nm. The scan direction is from surface to bulk, as indicated by the purple arrows in the figures. Note that while the ALD coating did not cover every surface of every particle, it was possible to obtain consistent results from several particles selected from the coated sample.

The onset energy shifted to higher energy in both coated and uncoated samples, showing that there is some variation of Mn oxidation state from surface to bulk present in both samples. Pairs of individual spectra from the two different electrodes at the 2nd to 10th depth are also presented in Figures S3a–i (Supporting Information), with four representative comparisons (2nd, 3rd first and last two spectra from the ten spectra) also shown in Figure 4c. We note here the spectra from the 1st step (in black in the figures) were omitted from the comparison, since the spectrum from the surface of uncoated sample did not show any signal from Mn, which may be due to CEI formation on the surface blocking the signal. The pairwise comparison shows that the differences between the two samples are more obvious at the surface and less noticeable when going into the bulk. This indicates the average oxidation state of Mn in the coated sample is higher than uncoated at the very surfaces of the particles. Upon scanning deeper from the surface, the difference in the oxidation states of Mn became less pronounced.

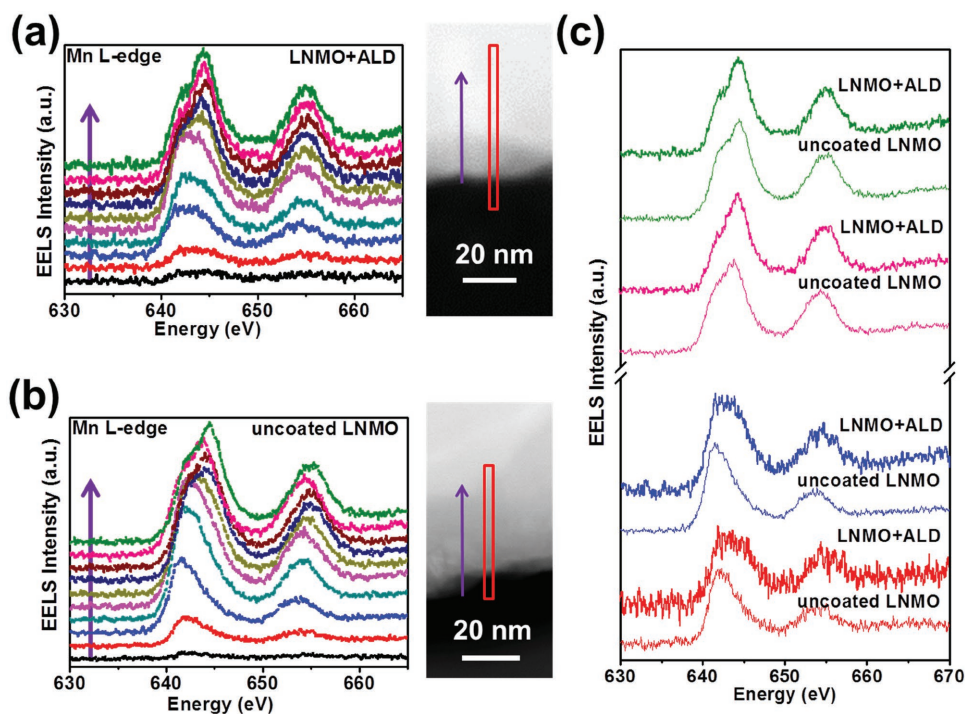


Figure 4. Mn L-edge spectra taken with EELS for particles from a) coated and b) uncoated electrodes after the 100th cycle. The STEM images showing the EELS scanning pathway were shown on the right side of the spectra. The step size in EELS scan was 1.5 nm and the first ten spectra from the surface of the particles were shown in (a) and (b). c) Comparison of Mn L-edge spectra taken at the 2nd, 3rd, 9th, and 10th steps shown in (a) (denoted as LNMO + ALD) and (b) (denoted as uncoated LNMO). The detailed comparisons of spectra taken at each depth were shown in Figure S3 (Supporting Information).

The results from the EELS measurements imply that the function of coating on $\text{LiNi}_{0.5}\text{Mn}_{1.5}\text{O}_4$ is to suppress the surface reaction that causes Mn^{2+} to form, but it does not entirely eliminate this phenomenon. This is also in agreement with the electrochemical data where an increase of the overpotential and charge transfer resistance was still observed in the cells with the coated electrodes, albeit to a lesser degree than in the ones with uncoated electrodes.

3. Conclusions

We studied the mechanism of the effect of ultrathin surface coatings on spinel $\text{LiNi}_{0.5}\text{Mn}_{1.5}\text{O}_4$. Complementary measurements including nanoscale STEM-EELS on the surface at the particle level, ensemble-averaged synchrotron XAS at the electrode level, and EIS and galvanostatic cycling at the cell level were combined in this study. The XAS results showed clear evidence that the ALD coating effectively suppresses the formation of Mn^{2+} on the surface of the electrodes, which occurs because of the reaction with the electrolyte on the surface of the $\text{LiNi}_{0.5}\text{Mn}_{1.5}\text{O}_4$ particles. The spatially resolved STEM-EELS showed that Mn^{2+} evolution occurs on the surfaces of both coated and uncoated $\text{LiNi}_{0.5}\text{Mn}_{1.5}\text{O}_4$ particles, but to a much lesser degree for the former. The ALD coating partially protects particle surfaces by avoiding direct contact of $\text{LiNi}_{0.5}\text{Mn}_{1.5}\text{O}_4$ and the electrolyte, and decelerates the impedance buildup, resulting in less apparent capacity fading. The electrochemical data acquired at the cell level is consistent with the XAS observations at the electrode level and the EELS results at the particle level. Our findings also suggest that an optimization of the coating thickness as well as coating material and coating process should be carefully studied in order to maximize the improvement achieved by surface modification of the battery materials. The results reported here can provide guidance for the development of strategies to improve battery performance by surface modification of cathodes.

4. Experimental Section

Material Synthesis: A solid-state reaction was used to synthesize $\text{LiNi}_{0.5}\text{Mn}_{1.5}\text{O}_4$ particles. Typically, nickel acetate ($\text{Ni}(\text{Ac})_2 \cdot 4\text{H}_2\text{O}$), and manganese acetate ($\text{Mn}(\text{Ac})_2 \cdot 4\text{H}_2\text{O}$) were mixed at a molar ratio of Ni: Mn = 1:3 and hand milled in a mortar. After heating at 500 °C for 5 h, lithium acetate ($\text{LiAc} \cdot 2\text{H}_2\text{O}$) was added to the mixture with a molar ratio of Li: Ni: Mn = 2.1:1:3 (5% excess Li source was added in order to make up for the volatilization of Li during calcination), and the mixture was heated to 500 °C for 5 h once more. The authors note here the amount of lithium acetate added in this step was critical. In addition, since the top portion of the mixture experienced more Li source volatilization, the total amount of precursors used in each round was fine-tuned to minimize the influence from Li source volatilization. The details can be found in the Supporting Information. After adding lithium acetate, the mixture was milled again and sintered at 950 °C for 10 h followed by annealing at 700 °C for 10 h. The product was naturally cooled in air.

ALD Process: ALD was performed on prefabricated electrodes using a home-made system. Pneumatic valves were used to control the pulse of the precursors and a tube furnace was used as reaction chamber. A programmable logic controller controlled the valves. Trimethylaluminum

(TMA) and H_2O were used as precursors. Ten cycles of ALD were performed at the temperature of 90 °C and pressure of 6×10^{-1} torr. Here one cycle of ALD referred to the deposition of H_2O and TMA each for one time. The electrodes were prepared using a traditional slurry casting method on Al current collectors. The weight ratio in the electrodes was active material: poly(vinylidene fluoride): carbon black = 8:1:1. The active material loading was about 3.5 mg cm^{-2} . After the ALD process, the electrodes were used directly without further annealing.

Electrochemical Measurements: CR 2032 coin cells were assembled with Li metal as counter electrodes. A 1.2 M solution of LiPF_6 in ethylene carbonate and dimethyl carbonate (DMC) (3:7) was used as the electrolytic solution. The batteries were cycled in the voltage range of 3.5–5 V. After a constant current charge, the batteries were charged at constant voltage of 5 V for either 30 min or until the current decreased to less than 0.01 mA, whichever came first. 1C rate is defined as 140 mA g^{-1} for this work. EIS were collected in a two-electrode configuration with AC voltage at 5 mV amplitude and a frequency range of 100–10 mHz. The batteries were fully charged and then rested overnight to reach equilibrium before the impedance test.

XRD: XRD measurements were performed on a Rigaku Ultima IV X-ray diffractometer with Cu as X-ray tube target. The operating voltage was 40 kV and current was 44 mA. The scan rate was 4° min^{-1} .

Synchrotron XAS: Batteries were disassembled in an argon filled glovebox after 35 cycles in either the charged or discharged state, as noted in the text and figures. Electrodes were rinsed with DMC and dried in the glovebox before being sealed into airtight bottles and transferred for the XAS measurements. XAS measurements were performed on the 31-pole wiggler beamline 10-1 at Stanford Synchrotron Radiation Light Source using a ring current of 350 mA and a 1000 L mm^{-1} spherical grating monochromator with 20 μm entrance and exit slits, providing $\approx 10^{11}$ ph s^{-1} at 0.2 eV resolution in a 1 mm^2 beam spot. All samples were attached to an aluminum holder using conductive carbon tape. Data were collected under high vacuum of 10^{-9} torr in a single load at room temperature. The sample drain current was collected for TEY. All spectra were normalized by the current from freshly evaporated gold on a fine grid positioned upstream of the main chamber.

STEM-EELS Measurements: The electrodes were in the fully discharged state when the batteries were opened up in the glovebox and rinsed with DMC. The particles were scratched off the electrodes and washed with N-Methyl-2-pyrrolidone to remove the poly(vinylidene fluoride) binder. The samples were dried at 50 °C under vacuum before taking the EELS measurements. STEM-EELS measurements were performed with a JEOL JEM-2100F Transmission Electron Microscope equipped with an electron energy loss spectrometer (Gatan Image Filter Quantum Standard Edition). The electron's accelerating voltage was 200 kV. The line scanning direction from surface to bulk had a step size of 1.5 nm.

Supporting Information

Supporting Information is available from the Wiley Online Library or from the author.

Acknowledgements

The authors would like to acknowledge the collaboration of this research with King Abdul-Aziz City for Science and Technology (KACST) via the Center of Excellence for Green Nanotechnologies (CEGN). The synchrotron X-ray portions of this research were carried out at the Stanford Synchrotron Radiation Lightsource, a Directorate of Stanford Linear Accelerator Center National Accelerator Laboratory and an Office of Science User Facility operated for the US Department of Energy Office of Science by Stanford University (No. DE-AC02-76SF00515). The STEM-EELS experiments were carried out at the Center for Electron

Microscopy and Microanalysis at the University of Southern California. The authors acknowledge the help from Dr. Steve Cronin's group for EIS measurements. Portions of the work carried out at Lawrence Berkeley National Laboratory were supported by the Assistant Secretary for Energy Efficiency and Renewable Energy, Office of Vehicle Technologies of the U.S. Department of Energy (DOE) under Contract No. DE-AC02-05CH11231. F.L. gratefully acknowledges Virginia Tech Department of Chemistry startup funds. X.F. and F.L. participated in designing the experiment. X.F. performed material synthesis, characterization, and electrochemical measurements. X.F. performed ALD coating with assistance of Y.C. X.F. prepared the samples for XAS characterization with assistance from F.L. F.L. D.N., and M.M.D. designed and performed the synchrotron XAS measurements. X.F. prepared the samples for EELS measurements with assistance from M.M. M.M. performed STEM and EELS experiments. X.F. prepared figures and wrote the paper with assistance from all authors. C.Z. supervised the project. All authors participated in discussion and review of the paper. The authors declare no competing financial interests.

Received: June 9, 2016

Revised: October 25, 2016

Published online: January 3, 2017

- [1] a) M. Armand, J. M. Tarascon, *Nature* **2008**, 451, 652; b) J. M. Tarascon, M. Armand, *Nature* **2001**, 414, 359; c) J. B. Goodenough, K. S. Park, *J. Am. Chem. Soc.* **2013**, 135, 1167.
- [2] a) J. B. Goodenough, A. Manthiram, *MRS Commun.* **2014**, 4, 135; b) J. B. Goodenough, Y. Kim, *J. Power Sources* **2011**, 196, 6688.
- [3] J. B. Goodenough, *Energy Environ. Sci.* **2014**, 7, 14.
- [4] a) A. Ulvestad, A. Singer, J. N. Clark, H. M. Cho, J. W. Kim, R. Harder, J. Maser, Y. S. Meng, O. G. Shpyrko, *Science* **2015**, 348, 1344; b) H. G. Jung, M. W. Jang, J. Hassoun, Y. K. Sun, B. Scrosati, *Nat. Commun.* **2011**, 2, 516.
- [5] a) Y. K. Sun, S. T. Myung, B. C. Park, J. Prakash, I. Belharouak, K. Amine, *Nat. Mater.* **2009**, 8, 320; b) Y. K. Sun, Z. H. Chen, H. J. Noh, D. J. Lee, H. G. Jung, Y. Ren, S. Wang, C. S. Yoon, S. T. Myung, K. Amine, *Nat. Mater.* **2012**, 11, 942; c) H. Wu, G. Chan, J. W. Choi, I. Ryu, Y. Yao, M. T. McDowell, S. W. Lee, A. Jackson, Y. Yang, L. B. Hu, Y. Cui, *Nat. Nanotechnol.* **2012**, 7, 309; d) N. Liu, Z. D. Lu, J. Zhao, M. T. McDowell, H. W. Lee, W. T. Zhao, Y. Cui, *Nat. Nanotechnol.* **2014**, 9, 187; e) J. Liu, A. Manthiram, *J. Electrochem. Soc.* **2009**, 156, S13; f) G. Alva, C. Kim, T. H. Yi, J. B. Cook, L. P. Xu, G. M. Nolis, J. Cabana, *J. Phys. Chem. C* **2014**, 118, 10596; g) S. Kuppan, H. Duncan, G. Y. Chen, *Phys. Chem. Chem. Phys.* **2015**, 17, 26471.
- [6] J. Liu, A. Manthiram, *Chem. Mater.* **2009**, 21, 1695.
- [7] a) N. Liu, H. Wu, M. T. McDowell, Y. Yao, C. M. Wang, Y. Cui, *Nano Lett.* **2012**, 12, 3315; b) Z. W. Seh, W. Y. Li, J. J. Cha, G. Y. Zheng, Y. Yang, M. T. McDowell, P. C. Hsu, Y. Cui, *Nat. Commun.* **2013**, 4, 1331; c) X. Xiao, J. Kim, Z. Liu, US Patent **2013**, 9034519; d) X. Xiao, M. W. Verbrugge, J. S. Wang, P. Liu, US Patent **2012**, 9059451; e) Y. S. Jung, A. S. Cavanagh, Y. F. Yan, S. M. George, A. Manthiram, *J. Electrochem. Soc.* **2011**, 158, A1298; f) I. D. Scott, Y. S. Jung, A. S. Cavanagh, Y. F. An, A. C. Dillon, S. M. George, S. H. Lee, *Nano Lett.* **2011**, 11, 414; g) Y. H. Liu, X. Fang, M. Y. Ge, J. P. Rong, C. F. Shen, A. Y. Zhang, H. A. Enaya, C. W. Zhou, *Nano Energy* **2015**, 16, 399; h) Y. H. Liu, X. Fang, A. Y. Zhang, C. F. Shen, Q. Z. Liu, H. A. Enaya, C. W. Zhou, *Nano Energy* **2016**, 27, 27.
- [8] Y. S. Jung, A. S. Cavanagh, L. A. Riley, S. H. Kang, A. C. Dillon, M. D. Groner, S. M. George, S. H. Lee, *Adv. Mater.* **2010**, 22, 2172.
- [9] J. Arrebola, A. Caballero, L. Hernan, J. Morales, E. R. Castellon, J. R. R. Barrado, *J. Electrochem. Soc.* **2007**, 154, A178.
- [10] J. Arrebola, A. Caballero, L. Hernan, J. Morales, E. R. Castellon, *Electrochem. Solid-State Lett.* **2005**, 8, A303.
- [11] H. B. Kang, S. T. Myung, K. Amine, S. M. Lee, Y. K. Sun, *J. Power Sources* **2010**, 195, 2023.
- [12] R. Alcantara, M. Jaraba, P. Lavela, J. L. Tirado, *J. Electroanal. Chem.* **2004**, 566, 187.
- [13] Y. K. Sun, Y. S. Lee, M. Yoshio, K. Amine, *Electrochem. Solid-State Lett.* **2002**, 5, A99.
- [14] H. M. Wu, I. Belharouak, A. Abouimrane, Y. K. Sun, K. Amine, *J. Power Sources* **2010**, 195, 2909.
- [15] J. G. Li, Y. Y. Zhang, J. J. Li, L. Wang, X. M. He, J. Gao, *Ionics* **2011**, 17, 671.
- [16] T. Y. Yang, N. Q. Zhang, Y. Lang, K. N. Sun, *Electrochim. Acta* **2011**, 56, 4058.
- [17] J. H. Cho, J. H. Park, M. H. Lee, H. K. Song, S. Y. Lee, *Energy Environ. Sci.* **2012**, 5, 7124.
- [18] X. Fang, M. Y. Ge, J. P. Rong, C. W. Zhou, *J. Mater. Chem. A* **2013**, 1, 4083.
- [19] X. Fang, M. Y. Ge, J. P. Rong, Y. C. Che, N. Aroonyadet, X. L. Wang, Y. H. Liu, A. Y. Zhang, C. W. Zhou, *Energy Technol.* **2014**, 2, 159.
- [20] a) H. M. Cho, M. V. Chen, A. C. MacRae, Y. S. Meng, *ACS Appl. Mater. Interfaces* **2015**, 7, 16231; b) J. Song, X. G. Han, K. J. Gaskell, K. Xu, S. B. Lee, L. B. Hu, *J. Nanopart. Res.* **2014**, 16, 2745.
- [21] X. Fang, Y. Lu, N. Ding, X. Y. Feng, C. Liu, C. H. Chen, *Electrochim. Acta* **2010**, 55, 832.
- [22] J. H. Kim, S. T. Myung, C. S. Yoon, S. G. Kang, Y. K. Sun, *Chem. Mater.* **2004**, 16, 906.
- [23] a) S. M. George, *Chem. Rev.* **2010**, 110, 111; b) X. B. Meng, X. Q. Yang, X. L. Sun, *Adv. Mater.* **2012**, 24, 3589; c) R. L. Puurunen, *J. Appl. Phys.* **2005**, 97, 121301.
- [24] Q. M. Zhong, A. Bonakdarpour, M. J. Zhang, Y. Gao, J. R. Dahn, *J. Electrochem. Soc.* **1997**, 144, 205.
- [25] J. Xiao, X. L. Chen, P. V. Sushko, M. L. Sushko, L. Kovarik, J. J. Feng, Z. Q. Deng, J. M. Zheng, G. L. Graff, Z. M. Nie, D. W. Choi, J. Liu, J. G. Zhang, M. S. Whittingham, *Adv. Mater.* **2012**, 24, 2109.
- [26] J. Lu, C. Zhan, T. P. Wu, J. G. Wen, Y. Lei, A. J. Kropf, H. M. Wu, D. J. Miller, J. W. Elam, Y. K. Sun, X. P. Qiu, K. Amine, *Nat. Commun.* **2014**, 5, 5693.
- [27] a) E. Peled, D. Golodnitsky, G. Ardel, *J. Electrochem. Soc.* **1997**, 144, L208; b) M. D. Levi, D. Aurbach, *J. Phys. Chem. B* **1997**, 101, 4630.
- [28] a) F. Lin, I. M. Markus, D. Nordlund, T. C. Weng, M. D. Asta, H. L. L. Xin, M. M. Doeff, *Nat. Commun.* **2014**, 5, 3529; b) F. Lin, D. Nordlund, T. C. Weng, Y. Zhu, C. M. Ban, R. M. Richards, H. L. Xin, *Nat. Commun.* **2014**, 5, 3358; c) X. S. Liu, D. D. Wang, G. Liu, V. Srinivasan, Z. Liu, Z. Hussain, W. L. Yang, *Nat. Commun.* **2013**, 4, 2568.
- [29] R. M. Qiao, Y. S. Wang, P. Olalde-Velasco, H. Li, Y. S. Hu, W. L. Yang, *J. Power Sources* **2015**, 273, 1120.
- [30] W. S. Yoon, M. Balasubramanian, K. Y. Chung, X. Q. Yang, J. McBreen, C. P. Grey, D. A. Fischer, *J. Am. Chem. Soc.* **2005**, 127, 17479.
- [31] F. Lin, D. Nordlund, I. M. Markus, T. C. Weng, H. L. Xin, M. M. Doeff, *Energy Environ. Sci.* **2014**, 7, 3077.
- [32] a) J. Ma, P. Hu, G. L. Cui, L. Q. Chen, *Chem. Mater.* **2016**, 28, 3578; b) J. F. Browning, L. Baggetto, K. L. Jungjohann, Y. Wang, W. E. Tenhaeff, J. K. Keum, D. L. Wood, G. M. Veith, *ACS Appl. Mater. Interfaces* **2014**, 6, 18569.
- [33] A. Jarry, S. Gottis, Y. S. Yu, J. Roque-Rosell, C. Kim, J. Cabana, J. Kerr, R. Kostecki, *J. Am. Chem. Soc.* **2015**, 137, 3533.

- [34] N. P. W. Pieczonka, Z. Y. Liu, P. Lu, K. L. Olson, J. Moote, B. R. Powell, J. H. Kim, *J. Phys. Chem. C* **2013**, *117*, 15947.
- [35] X. Fang, N. Ding, X. Y. Feng, Y. Lu, C. H. Chen, *Electrochim. Acta* **2009**, *54*, 7471.
- [36] M. X. Lin, L. B. Ben, Y. Sun, H. Wang, Z. Z. Yang, L. Gu, X. Q. Yu, X. Q. Yang, H. F. Zhao, R. Yu, M. Armand, X. J. Huang, *Chem. Mater.* **2015**, *27*, 292.
- [37] E. Y. Hu, S. M. Bak, J. Liu, X. Q. Yu, Y. N. Zhou, S. N. Ehrlich, X. Q. Yang, K. W. Nam, *Chem. Mater.* **2014**, *26*, 1108.
- [38] a) J. M. Zheng, M. Gu, J. Xiao, P. J. Zuo, C. M. Wang, J. G. Zhang, *Nano Lett.* **2013**, *13*, 3824; b) A. Boulineau, L. Simonin, J. F. Colin, C. Bourbon, S. Patoux, *Nano Lett.* **2013**, *13*, 3857.
- [39] A. Singer, A. Ulvestad, H. M. Cho, J. W. Kim, J. Maser, R. Harder, Y. S. Meng, O. G. Shpyrko, *Nano Lett.* **2014**, *14*, 5295.
- [40] D. C. Tang, Y. Sun, Z. Z. Yang, L. B. Ben, L. Gu, X. J. Huang, *Chem. Mater.* **2014**, *26*, 3535.
- [41] J. W. Kim, D. H. Kim, D. Y. Oh, H. Lee, J. H. Kim, J. H. Lee, Y. S. Jung, *J. Power Sources* **2015**, *274*, 1254.
-